EUROPEAN ENDODONTIC JOURNAL

ORIGINAL ARTICLE

Morphometric Analysis of Mandibular Incisors with Single Canal Systems Using A Developmental Automated Computational Framework

Abdulkadir Tasdelen[1], Mohamed Hadi Habaebi[2], Hoda Mohamed Abdelrazek Elnawawy[3], Hany Mohamed Aly Ahmed[4]

[1]Department of Software Engineering, Ankara Yıldırım Beyazıt University Faculty of Engineering and Natural Sciences, Ankara, Türkiye

[2]Department of Electrical and Computer Engineering, International Islamic University Malaysia Faculty of Engineering, Selangor, Malaysia

[3]Faculty of Dentistry, Universiti Malaya, Kuala Lumpur, Malaysia

[4]Department of Restorative Dentistry, Universiti Malaya Faculty of Dentistry, Kuala Lumpur, Malaysia

ABSTRACT

Objective: This study developed a computer vision–based framework for quantitative morphometric analysis of mandibular incisors with single root canals using axial video data obtained from micro-computed tomography (micro-CT).

Methods: Fifty extracted micro-CT scanned single-rooted mandibular incisors with single root canals (coded [1]TN[1] according to Ahmed et al. coding system) were included. After segmentation of the pulp space, video recordings were constructed using Mimics. The video frames were preprocessed through Gaussian filtering and segmented in the hue, saturation and value/brightness colour space domain. The contours were fitted with ellipses to compute morphometric descriptors, including aspect ratio (AR), roundness (R) and form factor. Aspect ratio–based classification was used to categorise canal cross-sections into 4 types (Round, Oval, Long Oval and Flattened). Automated AR measurements were validated against manual reference measurements of the same parameter at the cemento-enamel junction in 30 specimens, using Passing–Bablok and Deming regression, Bland–Altman analysis and the intraclass correlation coefficient; R and FF were not subjected to formal method comparison. Longitudinal trends along all thirds were visualised, and similarity measurement–based grouping comparisons were performed using dynamic time warping (DTW) clustering algorithm.

Results: The automated framework successfully processed 8334 axial frames. Within each root third, DTW clustering of AR trajectories resolved 3 morphological strata. Cluster 1 represented canals with the highest R (mean = 0.82) and lowest AR (mean = 1.39). Cluster 2 showed moderate ovality, while Cluster 3 exhibited the most complex morphology with the highest AR (mean = 2.84) and lowest R (mean = 0.40). Only 17 of the 50 specimens (34%) retained the same stratum in all 3 root thirds (mean adjusted Rand index 0.176), indicating that a canal's morphological class frequently changes along the root. Morphometric analysis revealed that canal complexity and flattening reached their peak in the middle third of the root.

Conclusion: This study introduces a robust and fully automated framework for quantitative assessment of canal morphology using axial videos. The findings highlight that mandibular incisors often harbour significant morphological complexity in the middle third, which may challenge standard instrumentation.

Keywords: Computer vision, mandibular incisors, medical image processing, morphological analysis, root canal profiling

Cite this article as: Tasdelen A, Habaebi MH, Elnawawy HMA, Ahmed HMA. Morphometric analysis of mandibular incisors with single canal systems using a developmental automated computational framework. *Eur Endod J*. 2026;11(10):500-516.

Corresponding authors:
Abdulkadir Tasdelen
✉ abdulkadirtasdelen@aybu.edu.tr
Mohamed Hadi Habaebi
✉ habaebi@iium.edu.my, Hany Mohamed Aly Ahmed
✉ hany_endodontist@hotmail.com

Received : April 29, 2026
Revision Requested: June 6, 2026
Last Revision Received: August 16, 2026
Accepted: August 18, 2026
Publication Date: October 21, 2026

DOI: 10.65717/eej.2026.26061

© 2026 The Author(s).
Licensee European Endodontic Journal
This article is licensed under the Creative Commons Attribution 4.0 International License (CC BY).

INTRODUCTION

Understanding the internal morphology of the root canal system is a fundamental prerequisite for successful endodontic treatment.[1] The shape, curvature and 3-dimensional complexity of root canals directly influence the effectiveness of cleaning, shaping and obturation procedures.[2] Mandibular incisors, in particular, exhibit highly variable canal anatomy, in which subtle cross-sectional variations may lead to incomplete debridement of the root canal system.[3]

HIGHLIGHTS

- A fully automated computer vision–based framework was developed for quantitative morphometric analysis of mandibular incisor root canals using axial micro-computed tomography video data.
- The proposed pipeline integrates hue, saturation and value/brightness-based segmentation, contour validation and ellipse fitting to extract aspect ratio, roundness and form factor across the entire canal length.
- Dynamic time warping clustering identified 3 distinct morphometric patterns, revealing significant anatomical variability among samples.
- The middle third of the root canal exhibited the highest morphological complexity and elongation across all clusters.
- The method provides a reproducible and high-throughput approach that may support improved understanding of canal anatomy and could potentially inform future studies on endodontic instrumentation strategies.

Conventional radiographic modalities provide only limited insights into these variations due to their 2-dimensional nature. Recent years have shown an exponential increase in the use of 3D imaging in laboratory and clinical settings.[4,5]

Recent advances in digital imaging and automated computational analysis have created new opportunities for morphological assessment, especially with the application of high-resolution images obtained from micro-computed tomography (micro-CT). The use of video imaging, obtained through the recording of serial axial sections along the tooth, provides continuous 2-dimensional frames that collectively capture the progression of canal geometry along its full length.[6] The axial videos offer a dynamic representation that can be processed to extract high-density morphometric data. However, such datasets require automated algorithms capable of isolating root and canal boundaries, quantifying shape descriptors and maintaining robustness against illumination changes, noise and anatomical variability.

Computer vision techniques, particularly those utilising colour-based segmentation and geometric modelling, have demonstrated strong performance in biomedical applications involving object boundary detection and quantitative shape analysis.[7] The hue, saturation and value/brightness (HSV) colour space, for instance, has been shown to offer greater resilience to lighting variability compared with Red-Green-Blue (RGB)-based segmentation, enabling consistent identification of dentine and root canal space.[7] When combined with contour detection and ellipse fitting methods, these computational tools can generate clinically meaningful descriptors such as aspect ratio (AR), roundness (R) and form factor (FF) that are widely used in anatomical and morphological research.

Despite increasing interest in digital endodontics, there remains a lack of fully automated computational frameworks integrating continuous morphometric extraction, longitudinal shape tracking and trajectory-based clustering of root canal morphology. Although several studies evaluated root canal morphology along larger portions of the canal using AR analysis, many investigations still rely on measurements obtained from selected anatomical levels, limiting continuous quantitative assessment along the entire root length.[5,8,9] The development of a robust algorithmic pipeline for video-based morphometric analysis may therefore offer a practical and reproducible approach that complements conventional slice-based measurement on the same micro-CT data.

In this study, the authors introduce a fully automated computer vision–based workflow designed to extract and analyse morphometric parameters from axial video sequences of micro-CT scanned mandibular incisors with single root canals. The framework integrates HSV-based segmentation, contour validation, ellipse fitting and aspect-ratio-driven classification across coronal, middle and apical root thirds. Additionally, dynamic time warping (DTW) and clustering analyses were employed to uncover underlying patterns and group-level behaviour among the samples. It should be emphasised that the individual computational components applied here—HSV thresholding, contour extraction, ellipse fitting and DTW—are established image-processing methods rather than artificial intelligence in the strict sense; the contribution of the present work lies in their integration into a single automated pipeline that converts an axial micro-CT video into a continuous morphometric trajectory and then groups those trajectories into reproducible morphological patterns. Mandibular incisors with a single canal were deliberately chosen as the simplest anatomical model in which to establish and validate this pipeline, since a single canal lumen guarantees exactly 1 canal contour per cross-section; this study is therefore intended as the methodological foundation for subsequent extension of the framework to multi-canal and multi-rooted configurations. By providing detailed quantification of geometric transitions along the canal length, this method aims to advance digital morphology research, support instrument design considerations and enhance anatomical understanding of mandibular incisors.

MATERIALS AND METHODS

Study Design

This study developed an automated computational framework for quantitative morphometric analysis of mandibular incisors with single root canals using axial video data obtained from micro-CT.

Sample Selection

An ethical approval was obtained from Universiti Malaya for this study (Approval no: DF RD2411/0075 (L); Date: 27.08.2024). A total of one hundred thirty-five extracted human mandibular incisors were initially screened. The teeth had been extracted for reasons unrelated to the present study and collected from an unidentified patient population (no consent was required since the samples were from unidentified individuals). The teeth were stored in saline until scanning. Teeth with complete root formation, no root fracture and without gross caries or previous root canal treatment were included in this study. Teeth with calcified canals and root resorption defects were excluded. After micro-CT scanning, a total of 50 extracted human mandibular incisors with single root canals (with the code ^{1}TN^{1} according to Ahmed et al coding system[10]) were selected from the main stock of one hundred thirty-five samples and included in

this study. The [1]TN[1] code denotes a single root carrying 1 canal that extends uninterrupted from a single orifice to a single apical foramen; specimens whose main canal divided, merged or terminated in more than 1 foramen were therefore excluded at this stage. One observer with at least 15 years of experience in root canal anatomy performed the selection of samples.

Accessory canals, lateral canals and apical ramifications (including apical deltas) were not applied as exclusion criteria, because these structures branch off the main canal and lie outside the object of measurement in the present framework. Their handling is determined by the contour validation rules described below: only contours fully contained within the root outline are retained, and where a cross-section yields more than 1 candidate contour, the largest valid contour is retained as the main canal lumen while smaller satellite contours corresponding to accessory branches are discarded. Every reported AR, R and FF value is therefore computed on the main canal lumen alone, and an accessory branch appearing in a given cross-section cannot alter the descriptor calculated for that frame. The prevalence of accessory anatomy within the sample was not separately tabulated, since it was not an outcome of the present analysis; this is acknowledged in the Limitations.

Because the framework generates an independent morphometric measurement for every axial frame rather than a single measurement per tooth, the 50 specimens yielded 8334 paired cross-sectional observations, which substantially increases the density of the morphometric data available for trajectory-based analysis.

Micro-Computed Tomography Imaging Protocol

The mandibular incisors were scanned using a high-resolution micro-CT technology (X-ray microscope, Xradia 520 Versa, Zeiss, Germany) at 80 kV, 88 µA (7 W), LE4 as a source filter, a 360° rotation with a 0.4 rotation step around the vertical axis, and an isotropic resolution of 25 µm. The data were then exported in international standard medical imaging format (Digital Imaging and Communications in Medicine [DICOM]). To create a 3D dataset, the acquired 2D scans were reconstructed using Materialise Mimics software, version 21.0 (Leuven, Belgium). The segmentation procedures were performed by an experienced operator (blinded for peer review) in root canal anatomy segmentation. Videos were obtained from the axial sections at the level of the cemento–enamel junction (CEJ) to the root apex after segmentation of the root canal space.

Image Processing and Video Generation

Each video was loaded using *cv2.VideoCapture()* and decomposed into individual frames, with metadata including frame count, frame index and spatial resolution recorded to monitor canal progression along the root. Prior to segmentation, *Gaussian blurring* with a 5×5 kernel was applied to suppress sensor noise, and frames were converted from the blue–green–red (BGR) to the HSV colour space to enable robust differentiation between the root structure and the canal. Segmentation was performed using 2 fixed HSV threshold–based masks: a root (dentine) mask defined by the range [0, 0, 80] to [180, 50, 200], and a canal mask defined by the range [80, 50, 50] to [130, 255, 255]. To refine the segmented regions, morphological dilation was applied using a 5×5 kernel with two iterations, followed by artifact removal in which connected components smaller than 10 px^2 were discarded. This preprocessing pipeline ensured accurate contour delineation and minimised segmentation noise across all frames.

Each axial video was generated from the segmented micro-CT volume in Materialise Mimics and exported in AVI format at 5 frames per second. Rendering mode, illumination and colour settings were held identical for all specimens, which is the requirement for the fixed HSV thresholds used in segmentation. Export frame size varied slightly between acquisition batches (1308 × 830, 1316 × 830, 1338 × 820 and 1350 × 830 pixels), so the pixel-to-millimetre scale was constant within a video but not identical across the dataset. This does not affect the reported measurements, because AR, R and FF are dimensionless ratios computed within a single cross-section and are therefore invariant to the display scale; no absolute length or area value is reported from the video data. No cropping, resizing or post-processing was applied to the exported videos. The axial plane was advanced continuously from the CEJ to the apex during recording, and the number of exported frames therefore varied between specimens. The axial interval represented by 1 video frame was computed for each specimen as its total canal length divided by its frame count, and ranged from 0.065 to 0.161 mm (median = 0.114 mm). Relative to the 25 µm isotropic reconstruction, 1 video frame therefore corresponded on average to approximately 4.6 reconstructed slices (range = 2.6-6.5) rather than to a single unique slice; the frames represent a regular subsampling of the volume along the canal axis rather than an exhaustive slice-by-slice export. Because all morphometric parameters reported here are dimensionless cross-sectional shape descriptors, and because trajectories were subsequently normalised to a common number of points per root third, this specimen-dependent sampling interval does not affect the reported values.

A total of 9222 frames were exported across the 50 videos (124-306 frames per specimen; 25-61 seconds duration at 5 fps). Of these, 888 frames (9.6%) contained no contour satisfying the validation criteria, occurring almost entirely at the extreme coronal and apical ends of the sequences where the canal lumen was not yet or no longer resolvable, and were excluded automatically; the remaining 8334 frames constituted the analysed dataset. Because video export operates at a fixed frame rate while the axial plane is advanced manually, a small number of consecutive frames may render the same axial position. In the present dataset, 305 of the 8334 analysed frames (3.7%; median 4.0% per specimen, maximum 8.2%) were exact duplicates of the preceding frame. Duplicated frames were retained, since they represent a genuine axial position rather than a measurement error, and their influence on the reported summaries is removed by the length normalisation described below, which resamples every trajectory onto a common number of points. No frames were discarded other than those failing contour validation.

Contours corresponding to the root and canal regions were extracted independently from their respective masks using *cv2.findContours()*.[11] To ensure anatomical validity, each detected canal contour was cross-validated against the corresponding root contour using *cv2.pointPolygonTest()*, thereby confirming that the canal boundary was fully enclosed within the dentin outline. Contours were retained for further analysis only if they satisfied the following criteria: an area of at least 10 px^2, the presence of a minimum of five boundary points, and complete containment of the canal contour within the root contour. Where a cross-section yielded more than 1 contour satisfying these criteria, the largest contour was retained as the main canal lumen and the remaining contours were discarded, so that exactly 1 canal contour contributed to the morphometric descriptors of each frame. For

all valid contours, ellipse fitting was performed using *cv2.fitEllipse()* to estimate geometric descriptors, including the major and minor axes, orientation angle and centroid coordinates.[12]

Ellipses were fitted to both the canal contour and the external root contour, and both are displayed in Figure 1. The 2 ellipses serve different purposes. The canal ellipse is the measurement object: its major and minor axes provide the diameters from which AR and R are computed, and its orientation angle records the buccolingual axis of the canal in each frame. The root ellipse contributes no reported morphometric parameter; it functions as an anatomical reference frame, providing a containment check that rejects frames in which segmentation has leaked beyond the dentine body, and an orientation reference against which the angular deviation of the canal axis can be monitored across consecutive frames so that any rotational drift introduced during video generation is detected. Both ellipses are shown in Figure 1 in order to document this quality-control step rather than to report a second set of measurements.

Distance transform was considered but not implemented, as contour-based ellipse fitting directly provided the target morphometric descriptors (AR, R and FF) without requiring skeletonisation-based analysis.

Validation for the Two-Dimensional Measurements for Quantitative Analysis of the Morphological Features

To validate the automated measurement framework, manual morphometric assessment was performed on a subset of 30 specimens and compared with the automated output (Figure 2) using the axial cross-section of the canal at the level of the CEJ. Formal method comparison was restricted to AR. Although Mimics also reports R and FF for the annotated cross-section (Figure 2), these were recorded for illustration only and were not subjected to regression or agreement analysis; the validation statistics reported below therefore apply to AR measurement alone. The CEJ was defined as the final coronal cross-section with visible enamel.[13] The CEJ is considered as a consistent landmark for the orifice of root canals in single-rooted teeth, which follows the coding system followed in this study.[10] A landmark-based level was required because a paired manual vs. automated comparison depends on both observers measuring the identical cross-section; levels defined as a distance from the apex depend on an operator-determined apical reference and would introduce landmark-identification error into the comparison itself. Manual annotation of all 8334 processed frames was not feasible, and the consequences of validating at a single anatomical level are addressed explicitly in the Limitations.

Morphometric Parameter Calculation

To assess the morphological profile of the root canals, the AR, R and FF were calculated as shown in Table 1.

Morphology Classification

Based on AR, each frame was assigned to 1 of 4 canal shape categories (Table 2).

The classification of Jou et al[14] is retained without modification, and the AR ranges given in Table 2 are those of the original scheme. In that scheme, the Round class is defined by the limiting value AR = 1.000. Because AR is measured here as a continuous variable at sub-pixel resolution, this value is effectively unattainable: the smallest AR recorded across the 8334 analysed cross-sections was 1.0018, and no frame reached 1.000 exactly. Applying the definition literally would

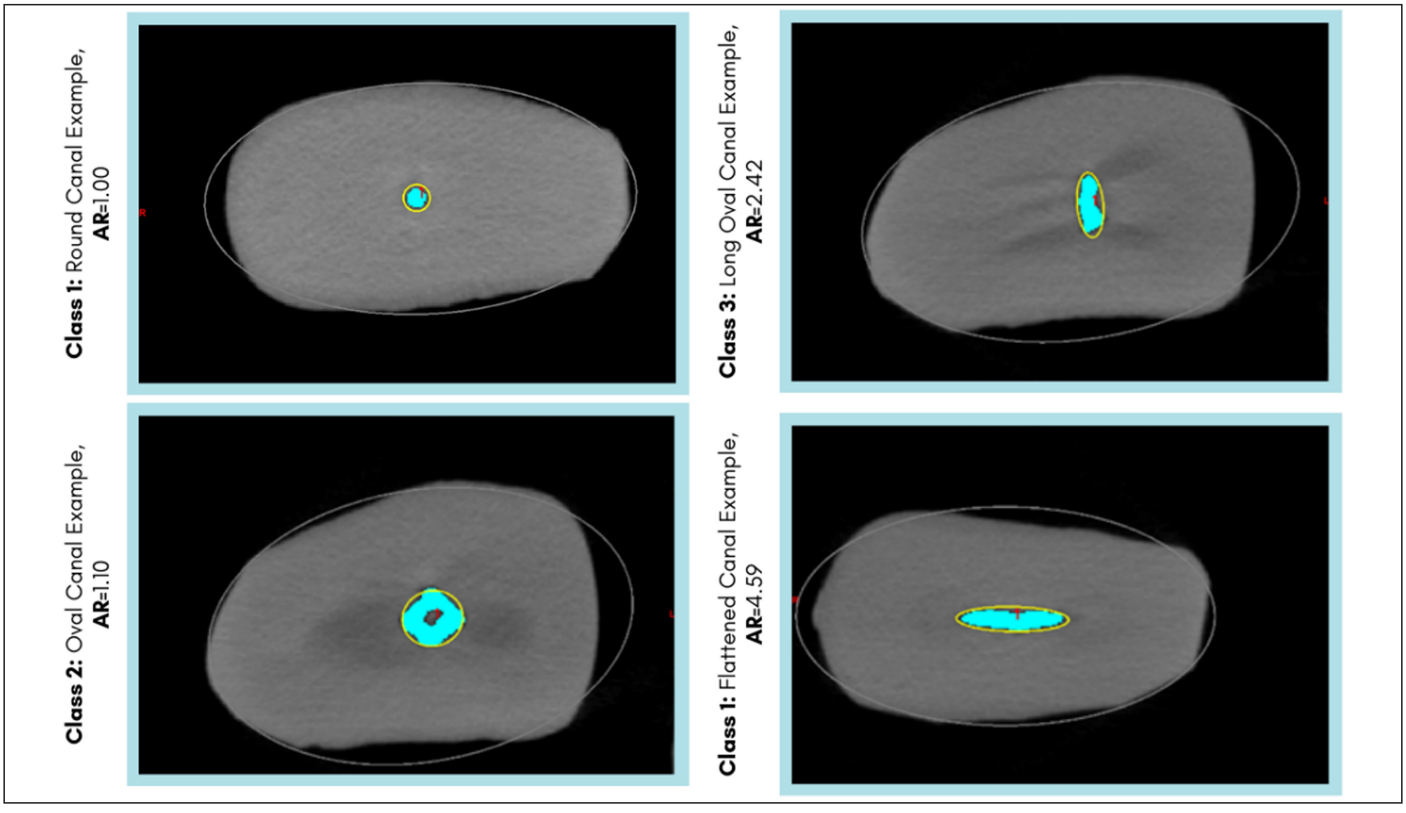


Figure 1. Representative examples of root canal cross-sectional morphologies based on AR.

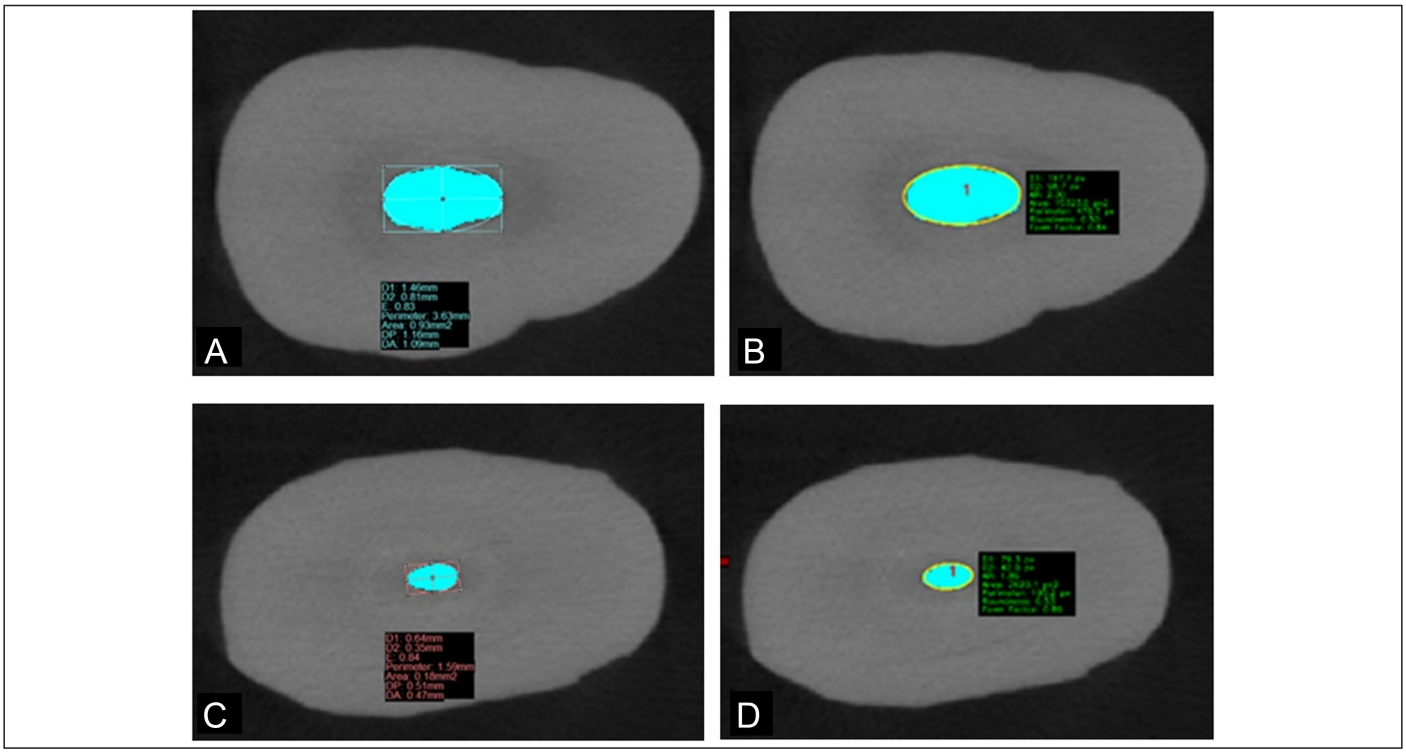


Figure 2. Measurements obtained from each of the Mimics (A and C) and automated measurement framework (B and D).

therefore leave the Round class permanently empty for reasons of measurement rather than of anatomy. An operational tolerance of AR ≤ 1.05 was adopted for frame assignment in the present study. This is a pragmatic convention rather than a measurement-resolved boundary: it is smaller than the mean absolute difference observed between manual and automated measurement (0.124), so genuinely oval cross-sections are not drawn into the Round class, but it is also smaller than the measurement uncertainty itself, and cross-sections falling within this band should therefore be read as approximately circular rather than as a category that can be distinguished from Oval with confidence. The underlying classification boundaries at AR = 2.0 and AR = 4.0, which separate the Oval, Long Oval and Flattened classes, are unchanged. The frame-level distribution of the 4 classes by root third is reported in Supplementary Table 4.

Representative examples of root canal cross-sectional morphologies based on AR are shown in Figure 1.

Clustering and Statistical Analysis

Data Storage and Visualisation

All computed frame-wise metrics were stored in Pandas DataFrames and exported to Excel with separate sheets for root and canal measurements.

Visual outputs included: 1. Cross-sectional parameter plots (area, axes lengths and AR). 2. Scatter plots and time-series graphs along canal length. 3. Automated AR classification summaries.

Dynamic Time Warping Clustering

To identify group-level morphological patterns, AR time series from all samples were clustered using the DTW method.

Because the number of axial frames per specimen varied with root length, each AR trajectory was first linearly interpolated onto a common normalised axis, so that all specimens were compared over the same relative canal length. Dynamic time warping was then applied on this normalised axis rather than a point-to-point Euclidean measure, because the relative depth at which a given morphological transition occurs varies between specimens: 2 canals may both reach their maximum elongation within the middle third but at different relative positions within it, and a point-to-point comparison would penalise this shift, whereas DTW aligns the corresponding transitions before quantifying their dissimilarity. The ability of DTW to successfully classify time series characterised by long-term trends and curvature, even in the presence of noise, has been validated in recent literature.[15,16] This alignment technique ensures that morphological transitions (e.g., changes in AR) are compared based on structural similarity rather than absolute spatial position.

Table 1. Definitions of Morphometric Parameters Used for Root Canal Shape Analysis[14]

Parameter	Definition
AR	Ratio of the major and minor diameters of the root canal.
R	$4.A/(\pi.[dmax]^2)$, where A is the area and *dmax* is the major diameter.
FF	$(4.\pi.A)/P^2$, where A is the area and P is perimeter. Elongation of individual objects results in smaller values of FF.

AR, aspect ratio; FF, form factor; R, roundness.

Table 2. Aspect Ratio–Based Classification of Root Canal Cross-sectional Morphology[14]

Class	Category	Aspect Ratio Range
1	Round	AR = 1.0 (operational: AR ≤ 1.05)
2	Oval	1.0 < AR < 2.0 (operational: 1.05 < AR < 2.0)
3	Long oval	2.0 ≤ AR < 4.0
4	Flattened	AR ≥ 4.0

AR, aspect ratio.

The number of valid frames varied between 37 and 98 per root third (113-294 per specimen; mean 166.7), reflecting differences in root length. For each root third, every specimen's trajectory was linearly interpolated onto the mean frame count of that third, which was 55 points in all 3 regions. Each specimen therefore contributed 55 normalised observations per third and 165 in total, giving 50 × 165 = 8250 normalised observations. Tables 3, 4 and 5 summarise these normalised observations, whereas the figure of 8334 refers to the raw valid cross-sections extracted before normalisation; the 2 numbers are used consistently in that sense throughout.

Clustering was performed exclusively using AR trajectories extracted from consecutive axial sections. Each sample was represented as a longitudinal AR time series. Pairwise DTW distances were computed and subsequently clustered using K-medoids. Solutions for $k = 2, 3, 4$ and 5 were generated from the identical distance matrix and compared before a final value was adopted. Because no single internal validity index is decisive for the clustering of morphological time series, and indices of this type are known to favour different solutions depending on cluster shape and separation, the number of clusters was determined by the convergence of 3 criteria: the population of the resulting clusters, since groups containing very few specimens cannot support morphological interpretation; the consistency of cluster assignment between root thirds, since a partition intended to describe canal-wide morphology should not reorganise completely from 1 root level to the next; and the nested behaviour of the partitions, that is, whether increasing k revealed an additional morphological phenotype or merely subdivided an existing group along the same morphological axis.[17] These criteria converged on $k = 3$, and the full comparison is presented in Supplementary Material. K-medoids was initialised with a fixed random seed (random_state = 42) to ensure deterministic partitions, and clusters were renumbered after fitting in ascending order of mean AR, so that Cluster 1 always denotes the least elongated group in every root third.

Clustering was carried out independently within each root third, so that the coronal, middle and apical partitions were derived from separate distance matrices. The resulting groups are therefore level-specific morphological strata: within a given root third, Cluster 1 denotes the least elongated group and Cluster 3 the most elongated, but a given specimen is not constrained to occupy the same numbered group at all 3 levels. Agreement of stratum membership between root thirds was quantified using the adjusted Rand index and is reported in the Results.

Workflow

A system-level workflow diagram was developed to illustrate the end-to-end processing stages, starting from micro-CT & DICOM input to final clustering and reporting. The pipeline consists of 6 main steps (Figure 3):

1. Input stage: Extraction of DICOM stacks in axial orientation and sequential frame-by-frame video generation.
2. Pre-processing: Application of Gaussian Blur (5x5 kernel) for noise reduction and HSV colour space conversion for lighting-resilient analysis.
3. Segmentation: Root-canal isolation through connected component analysis and least-squares ellipse fitting to model canal geometry.
4. Feature extraction: Computation of geometric metrics, including AR, R and FF.
5. Classification: Frame-wise AR tracking and DTW to calculate similarity matrices and align sequences of varying lengths.
6. Output & Reporting: K-Medoids clustering for anatomical categorisation, followed by visualisation via histograms/heatmaps and data export in Excel/CSV formats.

Computational Environment

All analyses were performed using Python 3.13.3 (Python Software Foundation, Wilmington, DE, USA) with OpenCV 4.12 for image processing and *tslearn* library for dynamic time-series comparison.[18-21] Data handling and statistical procedures utilised NumPy, Pandas and Matplotlib libraries.

Hardware specifications of the workstation: Intel® Core™ i9-13980HX processor (Intel Corp., Santa Clara, CA, USA), 16 GB DDR5 4800 MHz RAM, and NVIDIA® GeForce RTX™ 4070 graphics card with 8 GB GDDR6 memory (NVIDIA Corp., Santa Clara, CA, USA). Processing time per video averaged 1.5-2 minutes, depending on frame count and image resolution.

Table 3. The Mean, Standard Deviation and Median Values for the Three Clusters Related to AR

Cluster	Section	Mean	SD	Min	Max	Median	Count
Cluster 1	Coronal	1.246	0.207	1.004	2.391	1.201	935
	Middle	1.644	0.496	1.034	3.320	1.556	660
	Apical	1.392	0.294	1.016	3.224	1.316	990
Cluster 2	Coronal	2.001	0.440	1.072	3.363	1.967	825
	Middle	2.079	0.689	1.010	5.087	1.995	880
	Apical	1.853	0.506	1.020	3.750	1.757	1045
Cluster 3	Coronal	2.760	0.958	1.186	6.478	2.586	990
	Middle	3.489	0.975	1.530	6.424	3.307	1210
	Apical	2.845	0.968	1.034	6.199	2.910	715

AR, aspect ratio.

Table 4. The Mean and Standard Deviation for Roundness in Each Cluster

Cluster	Section	Mean	SD	Min	Max	Median	Count
Cluster 1	Coronal	0.821	0.114	0.420	0.996	0.832	935
	Middle	0.658	0.170	0.302	0.966	0.643	660
	Apical	0.745	0.131	0.311	0.984	0.760	990
Cluster 2	Coronal	0.526	0.124	0.298	0.932	0.508	825
	Middle	0.538	0.183	0.197	0.990	0.501	880
	Apical	0.580	0.151	0.267	0.980	0.569	1045
Cluster 3	Coronal	0.404	0.133	0.154	0.843	0.387	990
	Middle	0.310	0.086	0.156	0.653	0.303	1210
	Apical	0.407	0.174	0.162	0.967	0.345	715

Clusters are those derived from the AR trajectories; specimen membership and observation counts are therefore identical to Table 3.
AR, aspect ratio.

Method Comparison Statistics

To evaluate the agreement between the proposed framework and manual measurements of AR, a method comparison study was conducted. Two measurement approaches were examined: manual reference measurements (Mimics dataset) and measurements generated by the developed automated framework. Agreement, potential proportional and systematic differences, and overall reliability were assessed through a combination of regression-based and concordance analyses, with 95% CIs reported for all agreement statistics. Confidence intervals for the intraclass correlation coefficient (ICC) were obtained by the method of McGraw and Wong, those for Passing–Bablok parameters from the rank-based interval, those for Deming parameters by bootstrap resampling (10 000 replicates), and those for Bland–Altman bias and limits of agreement (LoA) by the standard parametric formulae.[22,23]

Proportional and systematic bias between the 2 methods was examined using Passing–Bablok and Deming regression. Agreement was assessed using the Bland–Altman approach, which provides mean bias and 95% LoA. Additionally, measurement consistency was evaluated using the ICC, absolute agreement and 2-way mixed model.

All computational analyses were implemented in Python. All processing parameters required to reproduce the pipeline are specified in the preceding subsections, including the HSV threshold ranges, the morphological kernel size and iteration count, the minimum contour area and boundary-point criteria, the library versions, and the clustering seed, so that the workflow can be re-implemented for comparable axial micro-CT datasets.

RESULTS

Pipeline Performance and Processing Accuracy

The automated computer vision pipeline successfully processed all 50 axial video datasets without requiring manual adjustments, yielding 8334 valid cross-sectional frames. Mean video length was 166.7 frames, and the average total processing time per sample dataset was < 120 seconds. Figure 4 shows morphometric analysis of Sample 1.

At the level of individual cross-sections, the AR-based classification placed 56.4% of coronal frames in the Oval class, 39.9% in the Long Oval class and 3.7% in the Flattened class. In the middle third, the proportion of Oval frames fell to 35.4% while Long Oval rose to 54.5% and Flattened to 10.2%, whereas the apical third was the most circular region, with 66.0% Oval, 31.4% Long Oval and 2.6% Flattened frames. The proportion of Flattened cross-sections was therefore approximately 3 times higher in the middle third than in the coronal third and approximately 4 times higher than in the apical third (Supplementary Table 4).

Table 5. The Mean and Standard Deviation for Form Factor in Each Cluster

Cluster	Section	Mean	SD	Min	Max	Median	Count
Cluster 1	Coronal	0.976	0.032	0.766	1.000	0.987	935
	Middle	0.908	0.090	0.618	1.000	0.930	660
	Apical	0.954	0.051	0.631	1.000	0.972	990
Cluster 2	Coronal	0.842	0.083	0.612	0.998	0.848	825
	Middle	0.829	0.120	0.441	1.000	0.842	880
	Apical	0.870	0.094	0.564	1.000	0.890	1045
Cluster 3	Coronal	0.722	0.137	0.357	0.989	0.730	990
	Middle	0.616	0.117	0.360	0.935	0.620	1210
	Apical	0.708	0.150	0.373	1.000	0.678	715

Clusters are those derived from the AR trajectories; specimen membership and observation counts are therefore identical to Table 3.
AR, aspect ratio.

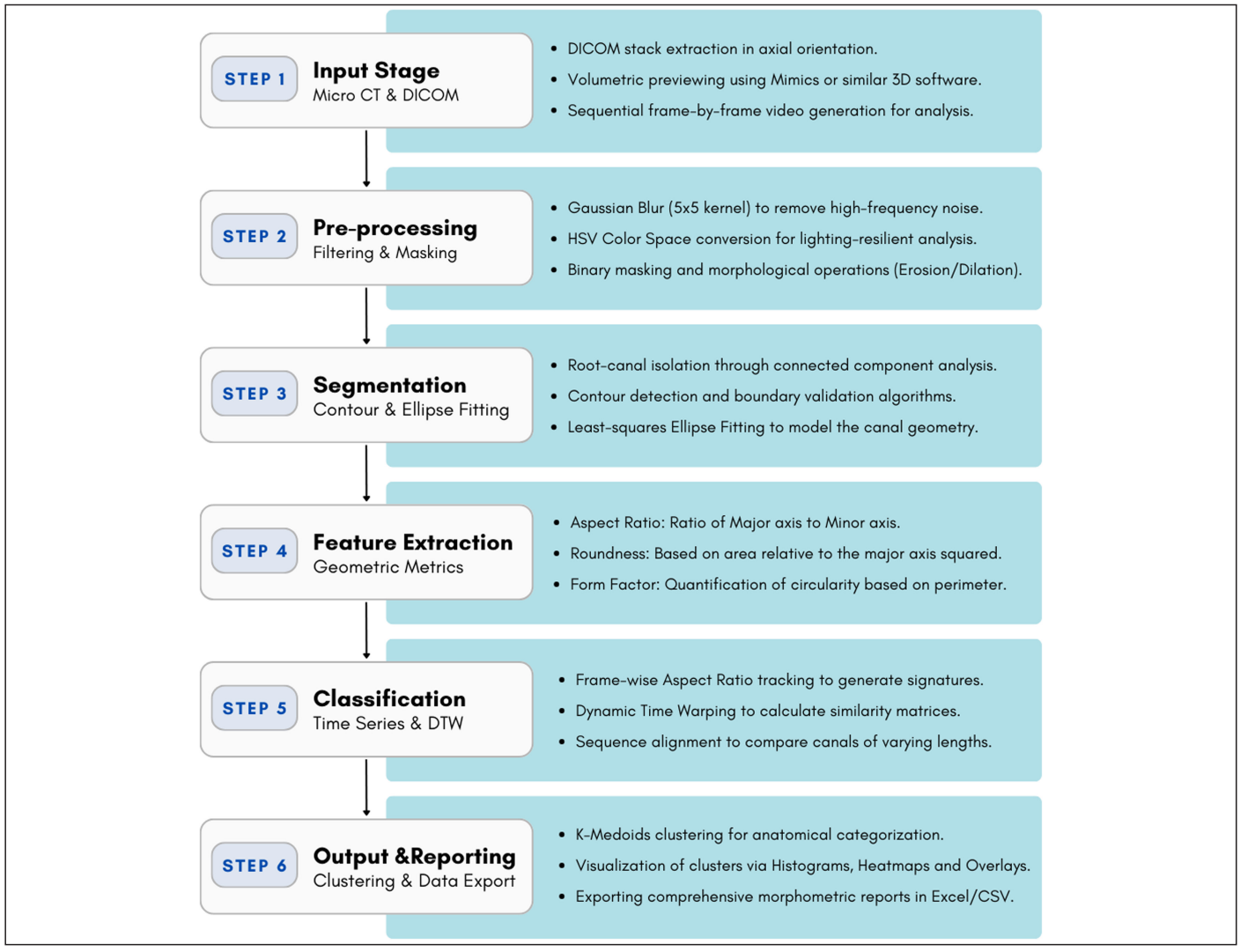


Figure 3. Workflow of the proposed automated morphometric analysis pipeline. The diagram demonstrates sequential stages from micro-CT data acquisition to feature extraction, clustering and visualisation. micro-CT, micro computed tomography.

Method Comparison and Agreement Metrics

A high concordance was observed between the manual and automated AR measurements. The ICC was 0.935 (95% CI = 0.858-0.969; n = 30), indicating good-to-excellent agreement between the 2 methods. The point estimate lies within the range conventionally described as excellent, although the lower confidence limit extends into the range described as good, and the interval should be interpreted with the moderate sample size in mind.[24]

Passing–Bablok regression yielded a slope of 1.119 (95% CI = 1.032-1.254) and an intercept of –0.129 (95% CI = –0.342 to –0.005). Because the CI for the slope excludes 1 and that for the intercept excludes 0, both a proportional and a small systematic difference between the methods are statistically supported. Deming regression, accounting for error in both axes, estimated a slope of 1.181 (95% CI = 0.966-1.330) and an intercept of –0.237 (95% CI = –0.478 to 0.082); these intervals include 1 and 0, respectively, so the proportional tendency is directionally consistent between the 2 models but reaches statistical support only under Passing–Bablok.

Bland–Altman analysis resulted in a mean bias of 0.069 (95% CI = 0.005-0.133), with 95% LoA from –0.267 (95% CI = –0.378 to –0.156) to 0.405 (95% CI = 0.294–0.516) and a standard deviation of the differences of 0.172. The automated framework therefore produced slightly higher AR values on average, and regression of the paired differences on their means confirmed a proportional component (slope = 0.162, $P = .009$). The magnitude of the difference is small relative to the measured range of 1.03-2.71, but it is systematic rather than random, and absolute AR values obtained by the 2 methods should not be pooled without applying the regression relationship reported above.

Figure 5 presents the regression-based comparison between manual and automatic measurements, and Figure 6 shows the Bland–Altman plot illustrating the measurement differences relative to the mean.

General Morphometric Trends Along the Root Canal

Aspect Ratio Progression

Aspect ratio values are summarised in Table 3. A 3-cluster solution was adopted (see Methods, DTW clustering, and Supplementary Material). In all 3 clusters, the mean AR rose from the coronal to the middle third and then declined towards the apex, with the middle third also showing the largest standard deviation and the widest

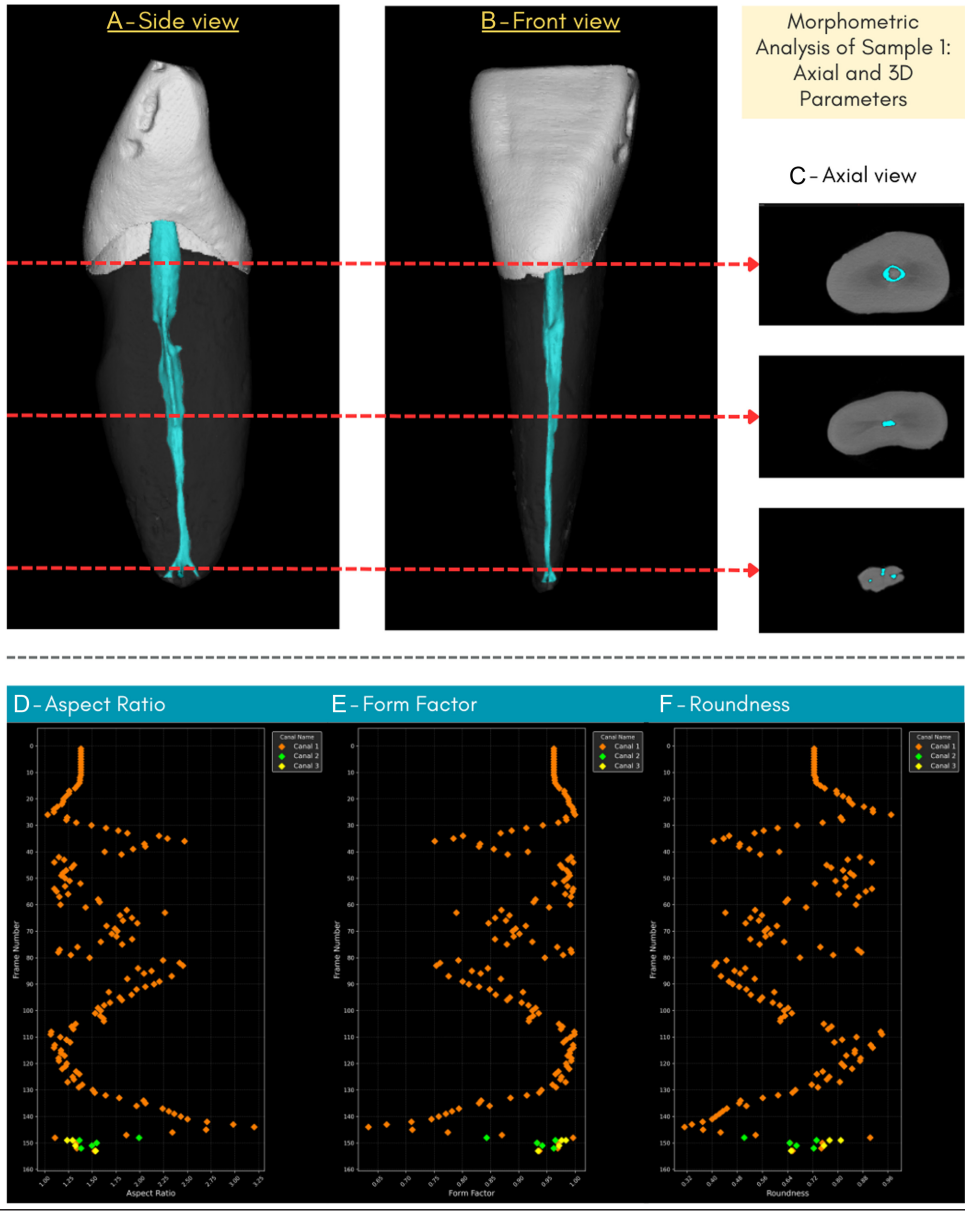


Figure 4. Morphometric analysis of Sample 1: Axial and 3D parameters: (A) side view and (B) front view of Sample 1 showing the reconstructed root canal morphology. (C) Representative axial cross-sections at 3 different levels along the root canal (coronal, middle and apical thirds). (D-F) Quantitative morphometric parameters plotted along the canal length, including (D) aspect ratio, (E) form factor and (F) roundness. Each point represents a cross-sectional measurement, colour-coded according to canal type.

min-max range. The absolute level of the profile differed between clusters (middle-third means: 1.644 in Cluster 1, 2.079 in Cluster 2 and 3.489 in Cluster 3), but the shape of the coronal–middle–apical profile was consistent across groups. Median values followed the same pattern. Despite the lower apical means, the apical third retained a broad distribution, particularly in Cluster 3, indicating that Long Oval and potentially flattened configurations persist near the apex.

These results indicate that canal cross-sections tended to become more elongated and oval-shaped towards the middle third of the root, where AR values reached their highest levels across all clusters. The middle region also demonstrated the greatest dispersion (highest standard deviations and min-max ranges), highlighting this region as the zone of maximum morphological heterogeneity. The apical third, despite showing reduced ARs relative to the middle level, retained a broad distribution range, suggesting persistent anatomical irregularity along the canal trajectory.

Figure 7 presents the analytical outcomes of the AR-based classification applied to mandibular incisors with a single root canal. Three distinct clusters (Clusters 1-3) were identified for the coronal, middle, and apical thirds, enabling comparative interpretation of morphological behaviour along the canal path. For each segment, AR distributions are visualised using histograms, whereas DTW-based heatmaps illustrate the similarity relationships within and between samples. Time-series overlays further reveal longitudinal trends and variability, and representative frames exemplify the characteristic geometrical profiles of each cluster. This multi-level comparison offers a comprehensive overview of cross-sectional morphological variation and

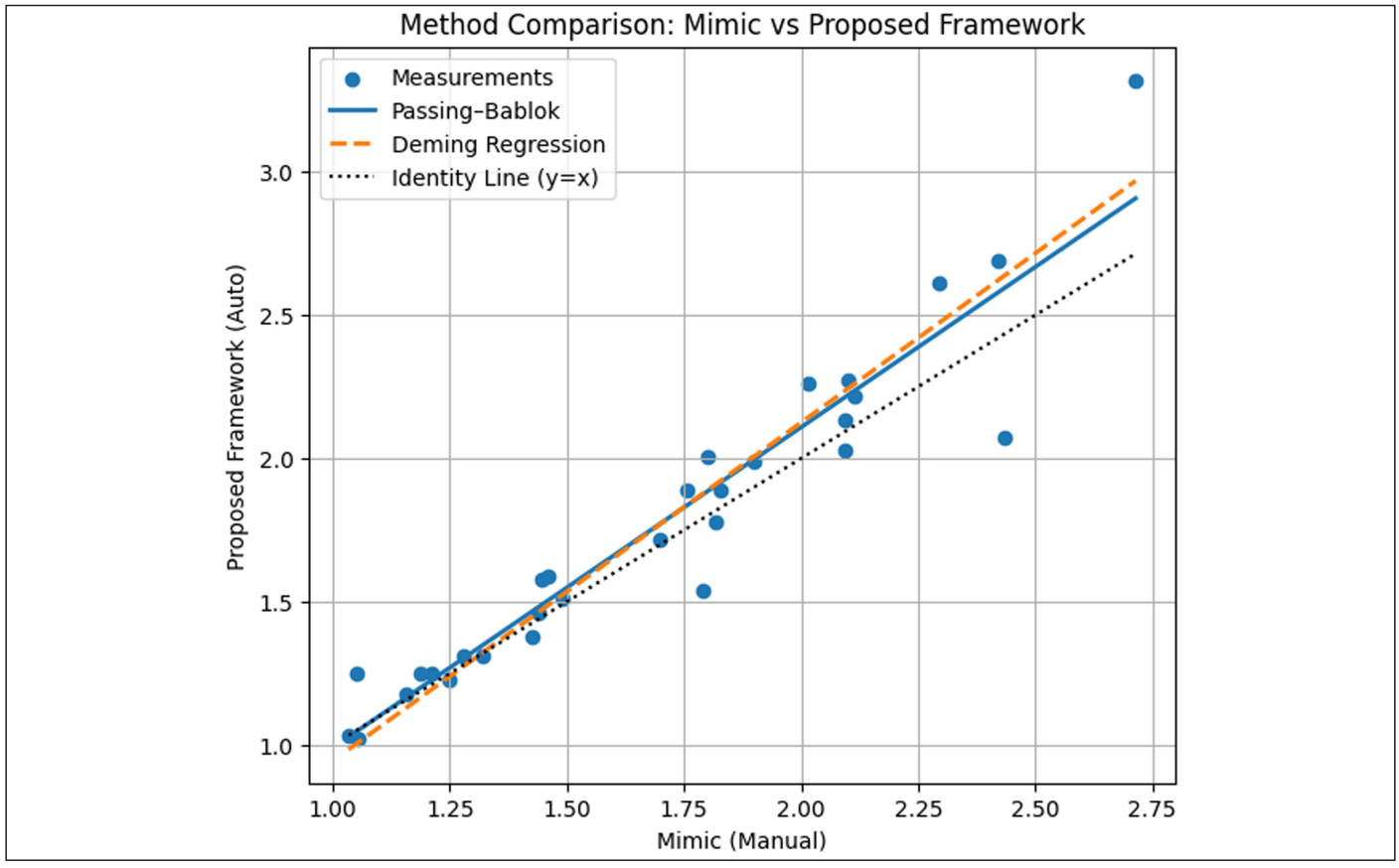


Figure 5. Method comparison between manual (mimic) and automatic measurement framework measurements using Passing–Bablok and Deming regression. Points represent paired observations, and regression lines illustrate the relationship between the 2 approaches relative to the identity line.

supports the use of AR as a reliable quantitative parameter for anatomical classification.

The heatmaps display the DTW-based pairwise distance matrices for each cluster, representing the temporal similarity of AR progression along the canal (Figure 8). Coronal sections demonstrated stronger diagonal alignment, indicating greater internal similarity and more uniform geometry among samples. In contrast, the middle and apical regions exhibited increased off-diagonal dispersion, reflecting higher morphological variability with depth. Cluster 1 showed the most compact structure, suggesting high similarity between samples within this group, whereas Cluster 3 presented the broadest spread, consistent with its wider AR range and higher standard deviation values observed in Table 3.

The time-series plots (Figure 8) illustrate the longitudinal AR behaviour for all samples within each cluster, where individual trajectories are shown as fine lines and the cluster mean is emphasised. Cluster 1 demonstrated stable patterns with minimal fluctuations, corresponding to predominantly rounded to mildly oval morphologies. Cluster 2 presented a moderate ascending profile, indicating a gradual increase in canal elongation towards the middle third. Cluster 3 displayed the largest variability with pronounced peaks and fluctuations, particularly within the middle region, confirming its heterogeneous and elongated morphology. Collectively, these visualisations show that morphometric complexity increases progressively from Cluster 1 to Cluster 3, with the middle third representing the zone of greatest geometric variation.

Because the partitions were derived independently within each root third, the stability of stratum membership along the root could be examined directly. Only 17 of the 50 specimens (34%) retained the same numbered stratum in all 3 thirds, and agreement between levels were low (adjusted Rand index: 0.342 = coronal-middle, 0.085 = middle-apical, 0.099 = coronal-apical; mean = 0.176). A canal classified as predominantly round in the coronal third was therefore frequently assigned to an intermediate or markedly flattened stratum at mid-root. This instability is a substantive result rather than a limitation of the clustering: it demonstrates quantitatively that cross-sectional morphology is not conserved along the canal, and consequently that assessment at any single anatomical level cannot represent whole-canal geometry.

The DTW-based similarity evaluation demonstrated notable differences across the 3 root segments. As presented in Table 6, the middle third exhibited the highest mean pairwise DTW distance (mean = 8.59, SD = 6.14) and the widest upper distribution range (P95 = 21.86; P99 = 28.23), indicating greater morphological variability within this region. The coronal third showed moderate dispersion (mean = 6.63, SD = 5.00), whereas the apical third revealed the lowest variation (mean = 5.66, SD = 4.12) and the narrowest range (maximum 20.91 vs. 32.44 in the middle third), reflecting a more uniform and stable canal geometry. Mean between-specimen dissimilarity in the middle third exceeded that of the apical third by 52% and that of the coronal third by 30%. These findings support the clustering output and heatmap visualisation, confirming that morphological fluctuations peaked predominantly in the middle region rather than towards the apex.

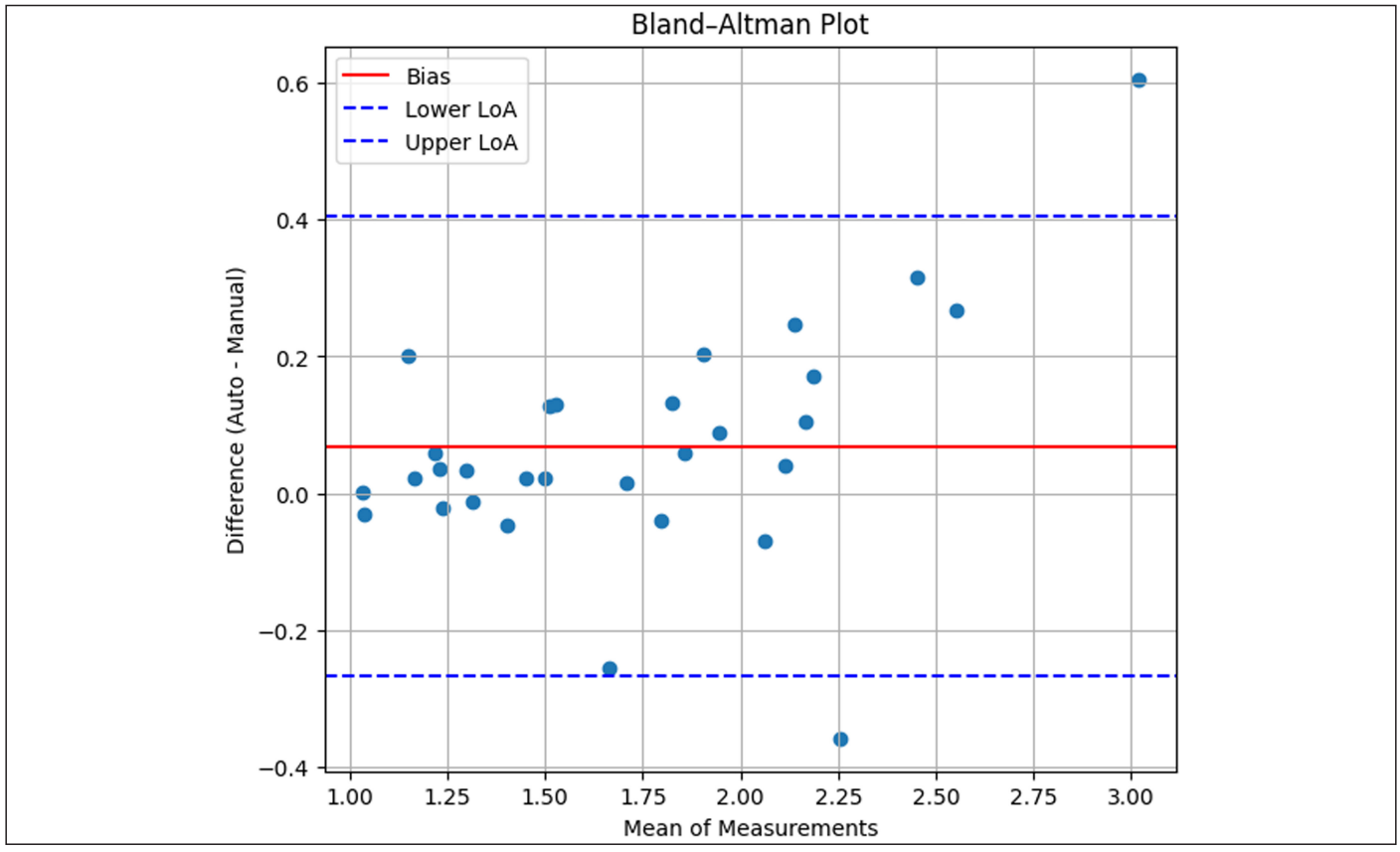


Figure 6. Bland–Altman plot of the difference vs. the mean of paired measurements. The central line indicates mean bias, whereas dashed lines represent the 95% LoA. LoA, limits of agreement.

To facilitate low-dimensional visualisation of the DTW-based morphometric similarity patterns, principal component analysis (PCA) was applied to the distance-based feature representations derived from AR time series. Principal component analysis was used solely as a dimensionality reduction and visualisation tool, allowing projection of high-dimensional DTW-derived features onto the first 2 principal components (Figure 9). This enabled visual assessment of cluster separability across coronal, middle, and apical thirds without influencing the clustering process itself.

Roundness and Form Factor

Roundness values, computed for the same AR-derived clusters, are presented in Table 4. Cluster 1 retained the highest circularity at every level, Cluster 3 the lowest, and Cluster 2 an intermediate position, so that the ordering established by AR was preserved by an independent shape descriptor. In Clusters 1 and 3, R followed a non-linear course, reaching its minimum in the middle third (0.658 and 0.310, respectively) and recovering apically (0.745 and 0.407), whereas Cluster 2 increased modestly and monotonically from coronal (0.526) to apical (0.580). Roundness therefore does not follow a uniform coronal-to-apical decline, and the level at which flattening is greatest is cluster-dependent.

Form factor values, computed for the same AR-derived clusters, are given in Table 5 and reproduce the same cluster hierarchy (Cluster 1 > Cluster 2 > Cluster 3 at every level), with the minimum again occurring in the middle third of each cluster (0.908, 0.829 and 0.616, respectively) and partial recovery apically. Compared with R, FF separated the clusters more consistently at every root level and showed a more pronounced apical recovery. The convergence of 3 descriptors computed on the same partition—AR, R and FF all reaching their least compact values in the middle third—indicates that the mid-root peak reflects the cross-sectional geometry itself rather than an artefact of any single metric.

DISCUSSION

Recent micro-CT studies have shown wide variations in the root canal anatomy of mandibular incisors.[13,24-27] The results align closely with previous micro-CT reports, which describe oval and Long Oval canal shapes as common configurations in mandibular incisors.[3,28] The present study expands this perspective by providing continuous frame-based morphometric evaluation rather than discrete slice measurements, allowing observation of shape transitions along the entire canal pathway. The findings showed that the middle third exhibited the greatest dimensional complexity, with AR and variability reaching maximum values in this region across all clusters, followed by a reduction towards the apical third. This observation emphasises that canal geometry is not uniformly progressive, but rather fluctuates along the root in a segment-dependent manner. This is consistent with the results of a recent study that showed pronounced anatomical asymmetry in mandibular incisors, particularly in the middle and coronal thirds, resulting in limited correspondence between conventional nickel–titanium (NiTi) instruments and the major canal diameter.[26]

The apparent divergence between R and FF values is expected and reflects the different geometric properties captured by each metric. Roundness is defined as $4A/(\pi \cdot d^2max)$ and is primarily sensitive to the

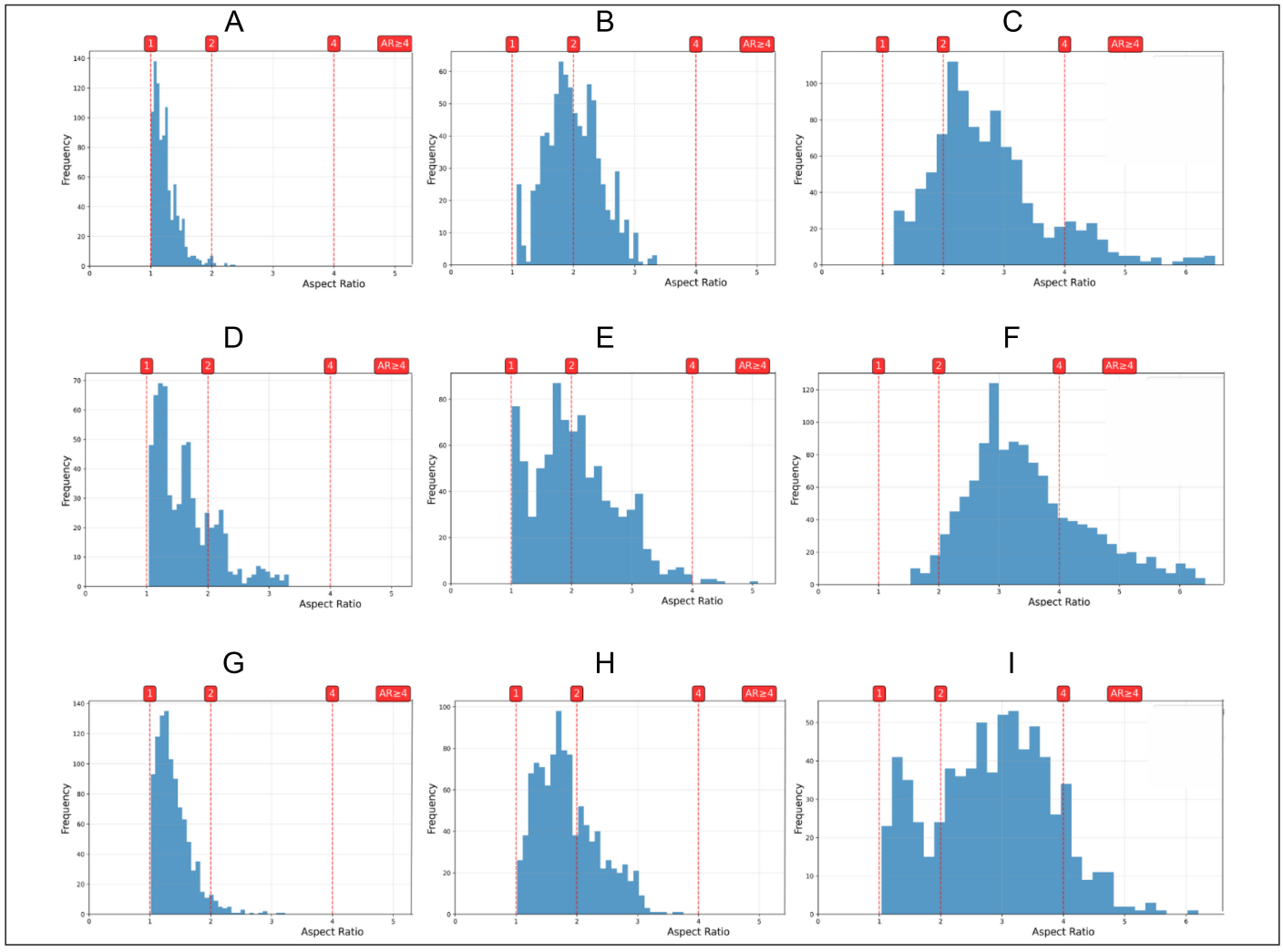


Figure 7. Distribution of AR values across 3 clusters for different anatomical thirds of the root canal. The rows represent anatomical segmentation (coronal, middle and apical thirds), whereas the columns represent the 3 clusters identified in the dataset. Subfigures (A–C) correspond to the coronal third, (D–F) to the middle third and (G–I) to the apical third. AR, aspect ratio.

relationship between area and major diameter, making it particularly responsive to elongation. Form factor, defined as $4\pi A/P^2$, additionally incorporates perimeter complexity and therefore reflects global boundary compactness and shape regularity. In highly flattened or irregular cross-sections—such as those characteristic of the mid-root region in Cluster 3—the 2 metrics may diverge because elongation may increase without a proportional increase in perimeter complexity (or vice versa). This divergence should therefore be interpreted as complementary morphological information rather than measurement inconsistency.

From a morphological perspective, the 3 DTW-derived groups are best understood as level-specific morphological strata rather than as whole-tooth phenotypes. Within any given root third, Cluster 1 corresponds to a predominantly round configuration, with the lowest AR and the highest R and FF; Cluster 2 to an intermediate or transitional configuration; and Cluster 3 to a markedly elongated, flattened configuration with the highest AR and the widest dispersion. This ordering was reproduced at every root level and by all 3 descriptors, which supports the strata as a consistent description of cross-sectional geometry. What the data do not support is the extension of these labels to the tooth as a whole: with only 34% of specimens retaining the same stratum across all 3 thirds and a mean adjusted Rand index of 0.176, the strata characterise a canal at a given level rather than classifying the canal in its entirety. The practical implication is that morphological grouping in comparative endodontic research should specify the root level at which it was determined, and that a single-level classification should not be carried forward as a property of the whole canal.

From a clinical standpoint, recognition of regions with increased elongation or flattening is important for instrumentation strategy design. Rotary and reciprocation systems frequently retain a fixed cross-sectional geometry, which may limit contact with the walls of Long Oval or flattened canals and predispose to untouched recesses, harbouring debris and biofilm.[29,30] The quantitative parameters obtained in this study could potentially inform future instrument design and irrigation strategies in studies specifically designed to address these outcomes. Additionally, continuous geometric mapping along the canal axis may contribute to guiding clinicians regarding irrigation dynamics, taper selection, and areas where enhanced cleaning or supplementary activation may be required. A recent study characterised the morphology of mandibular incisor root canals and evaluated their correspondence with commonly used NiTi instruments.[26] The findings demonstrated a gradual increase in both the minor and major canal diameters from the apical towards the coronal portion

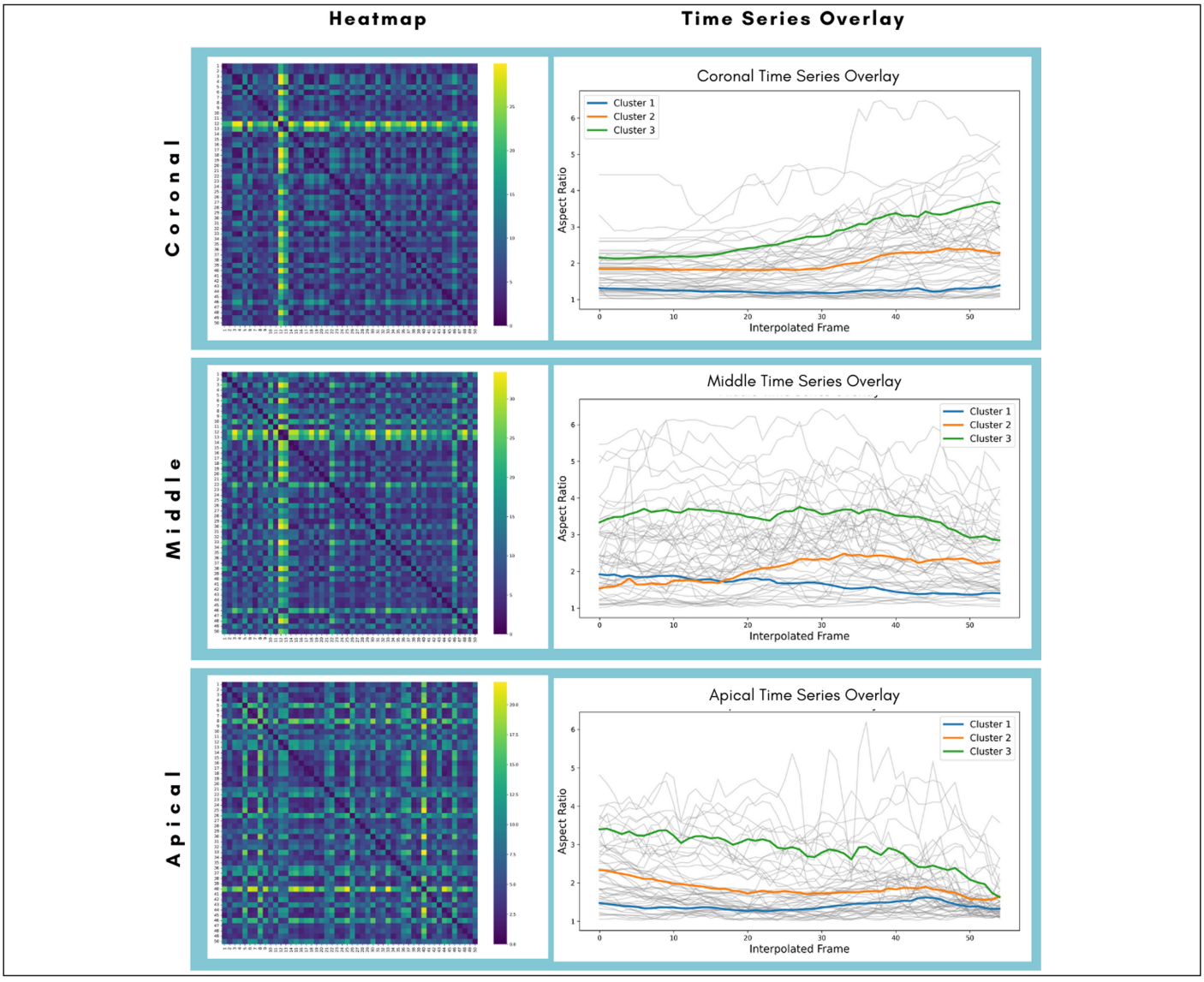


Figure 8. DTW distance heatmaps and time-series overlays illustrating similarity patterns between samples across clusters. Colour scale represents DTW distance with a constant offset of +1. DTW, dynamic time warping.

of the root canal. However, the expansion of the major diameter was particularly evident between the middle and coronal thirds. Canal morphology also varied along the root length, with round-shaped canals occurring most frequently in the apical third, whereas Long Oval configurations predominated in the middle and coronal regions. Although the minor canal dimension can often be addressed through the selection of instruments with suitable tip sizes and tapers, conventional constant-taper NiTi instruments are generally unable to adequately prepare the larger major canal dimension. Furthermore, the weak association observed between minor and major diameters suggests that enlargement in a single dimension does not necessarily result in proportional modification of the canal's overall geometric form.

Table 6. DTW Similarity Statistics Across Coronal, Middle, and Apical Thirds of the Root Canals

Section	Min	Max	Mean	SD	Median (P50)	P95	P99
Coronal	0.24	28.94	6.63	5.00	5.47	16.15	26.40
Middle	0.78	32.44	8.59	6.14	6.91	21.86	28.23
Apical	0.37	20.91	5.66	4.12	4.28	13.77	17.01

Middle third exhibited the highest DTW values indicating greater morphological variability, while the apical third demonstrated the lowest variation with the highest internal similarity. Lower DTW values indicate higher morphological similarity along the canal pathway. Statistics are computed on the raw DTW distance matrix using the 1225 unique specimen pairs (upper triangle), excluding self-distances and duplicated pairwise comparisons.
DTW, dynamic time warping.

It is important to state the epistemic status of these observations. The present study measured canal geometry only; it did not perform, simulate or evaluate any preparation, irrigation or obturation procedure, and no conclusion regarding instrument selection, taper or irrigation protocol follows from the data reported here. The morphometric descriptors are offered as inputs to studies designed to test those outcomes, and the correspondence between canal geometry and untouched canal wall reported for oval canals of mandibular incisors indicates that such studies are feasible using precisely the parameters quantified in this framework.[31]

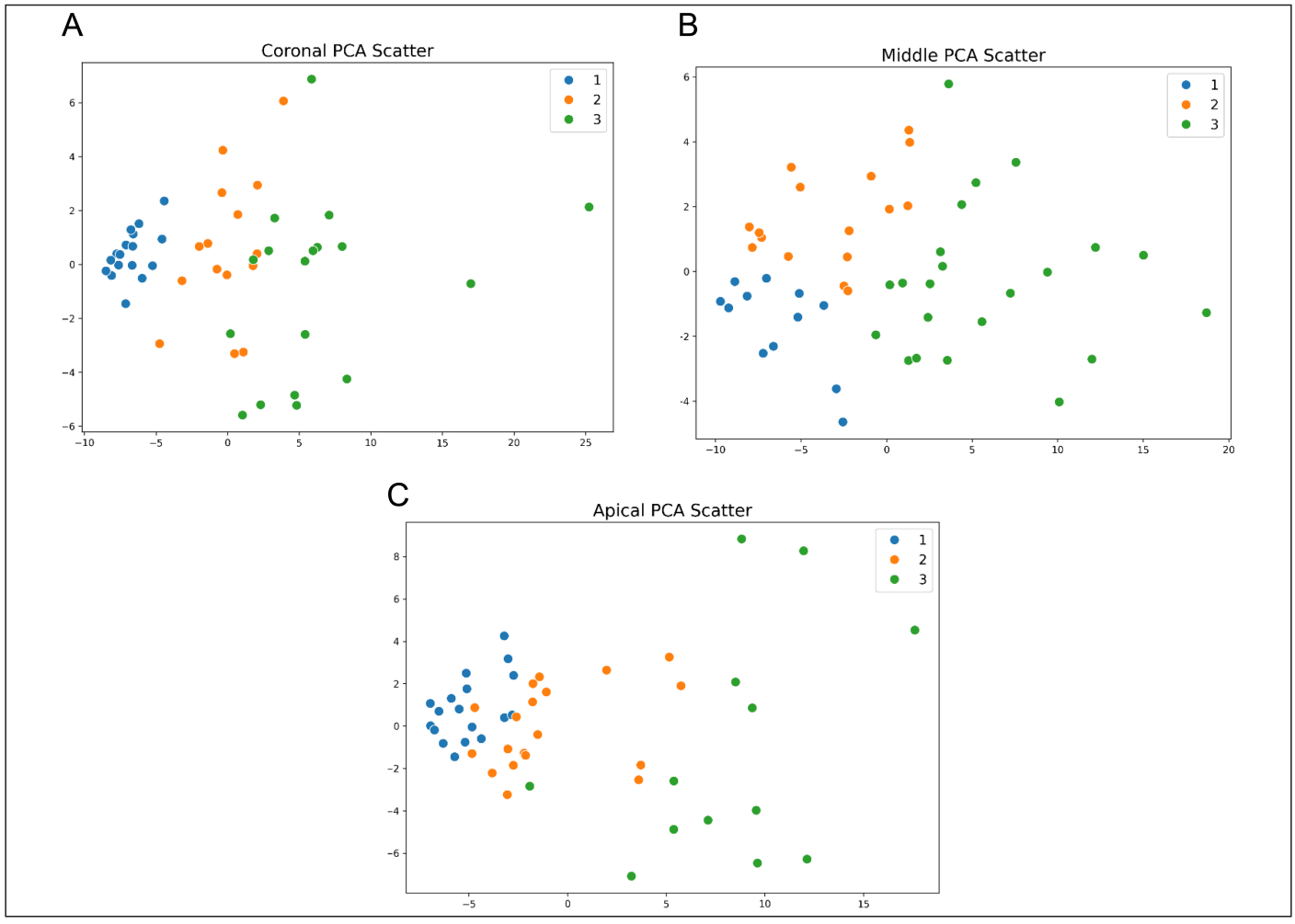


Figure 9. PCA scatter plots illustrating the spatial separation of DTW-based morphometric clusters across different anatomical levels of the root canal. Panels: (A) coronal, (B) middle and (C) apical thirds are presented. Each data point represents an individual sample projected onto the first 2 principal components derived from AR time-series features. The middle third demonstrates the most distinct cluster separation, indicating increased morphological variability, whereas partial overlap in the apical region reflects comparatively more homogeneous canal geometry. AR, aspect ratio; DTW, dynamic time warping; PCA, principal component analysis.

The proposed computer vision–based analysis framework may offer several practical advantages over conventional section-based approaches, although the 2 approaches were not compared experimentally in the present study and the framework is intended to complement rather than replace volumetric micro-CT analysis. Unlike isolated micro-CT slice measurements taken at fixed apical distances, axial video sequences may provide uninterrupted morphometric information, enabling detection of subtle geometric transitions that would otherwise remain unobserved. Hue, saturation, and value/brightness-based segmentation improved boundary separation robustness and reduced sensitivity to brightness differences, allowing stable contour extraction throughout the dataset. This robustness was established on the present dataset, in which all input videos were generated under uniform rendering settings from a single segmentation software; performance under different acquisition or rendering conditions has not been tested. High automation minimised operator dependency, reduced measurement subjectivity and demonstrated rapid processing performance (<2 minutes per sample), supporting the suitability of the method for large dataset applications and standardisation in research workflows. It should be emphasised that the workflow is not an imaging modality in its own right and does not remove the need for micro-CT acquisition; it operates on rendered axial sections derived from an existing micro-CT dataset. Its practical advantage is that, once the videos have been generated, the analysis requires no specialist volumetric software, which may facilitate use in educational and pre-clinical settings.

Ellipse fitting served as an efficient geometric approximation technique for deriving AR, R and FF; however, it inherently simplifies highly irregular morphology. Ribbon-like, extremely flattened canal outlines may not be fully represented by an ellipse model, particularly near the mid-root where variability peaked. Despite this, the continuous statistical pattern across clusters suggests that elliptical modelling captured the dominant structural characteristics sufficiently for classification and comparative analysis. Future implementation of spline-based boundary modelling or Fourier-shape descriptors may improve accuracy in irregular morphologies.

The clustering behaviour obtained using DTW analysis highlights the capacity of time-series–based similarity modelling to identify morphological patterns that are not evident in static measurements. Dynamic time warping enabled alignment of canals with varying lengths, improving trajectory-based comparison and producing 3 reproducible morphometric behaviour groups. Cluster 1 exhibited

low ARs and high circularity metrics, Cluster 3 displayed markedly elevated ARs with broader distribution ranges, and Cluster 2 consistently represented a transitional morphology between these groups. These outcomes support the interpretability of AR-based classification and demonstrate that temporal shape evolution can serve as a strong anatomical discriminator, consistent with the advantages of DTW in capturing structural variation over continuous sequences as noted by Glock et al.[16]

The DTW statistics further verified that the middle third represents the zone of greatest geometric heterogeneity along the canal pathway (mean pairwise DTW distance 8.59, SD 6.14, in the middle third, compared with 6.63, SD 5.00, coronally and 5.66, SD 4.12, apically; Supplementary Table 5). Mean between-specimen dissimilarity in the middle third exceeded that of the apical third by 52% and that of the coronal third by 30%. Increased temporal dissimilarity in this region suggests irregular canal outlines and dimensional transitions that may challenge mechanical instrumentation. The lower DTW spread in the apical third indicates a relatively more consistent morphology, with both the lowest mean and the narrowest range (maximum 20.91 vs. 32.44 in the middle third), while the coronal region demonstrated intermediate behaviour. These outcomes highlight the importance of enhanced shaping strategies and irrigation activation in the middle third, where untouched recesses and flattening are most likely to occur.

It is important to highlight that accessory canals, lateral canals and apical deltas were not considered in this study. Because the contour validation rules retain only the main canal lumen, such structures cannot contribute to the descriptors reported here; however, this also means that the present results describe the geometry of the main canal alone and should not be read as a complete account of the root canal system of these specimens. Quantifying accessory anatomy and relating it to the main-canal trajectory would require a multi-contour version of the pipeline in which each contour is tracked separately and branching events are detected explicitly.

Several limitations should be acknowledged. First, formal method comparison was performed for AR only and at a single anatomical level, the CEJ; R and FF were computed by the framework but were not validated against manual measurement, so the agreement statistics reported here should not be generalised to those 2 descriptors. Although agreement at that level was excellent (ICC = 0.9348), the principal contribution of the framework is continuous evaluation of the whole canal, and agreement at one level does not by itself establish equivalent accuracy in the middle and apical thirds, where the canal is smaller, the contrast between canal and dentine is lower, and the outline is more irregular; the proportional bias identified in the regression analysis may also behave differently in those regions. Multi-level validation, with paired manual measurements at defined coronal, middle and apical levels, is the principal methodological priority for subsequent work and is planned as part of the extension of this framework to multi-canal configurations. Second, the fixed HSV segmentation threshold was effective for this dataset but may require adaptive optimisation for videos acquired under different illumination or contrast conditions. Third, the ellipse approximation simplifies boundaries, potentially under-representing irregular forms; ribbon-shaped or figure-of-eight outlines are reduced to their best-fitting ellipse, so the ARs reported for the most flattened mid-root sections should be read as a conservative estimate of true morphological irregularity rather than as an upper bound. Fourth, the clustering solution ($k = 3$) was selected by the convergence of cluster population, cross-level consistency and nested structure within this dataset rather than by a single internal validity index (Supplementary Material), and the three strata require confirmation in an independent sample before being treated as generalisable anatomical categories. In addition, because the partitions were computed separately for each root third, the numbered strata are comparable in meaning but not in membership across levels; any comparison of a specimen between root thirds must therefore be made on the underlying morphometric values rather than on the stratum label. Finally, this study focused exclusively on single-root, single-canal mandibular incisors. This restriction was a deliberate design decision rather than an oversight: a single canal lumen guarantees exactly 1 contour per cross-section, which is the condition under which frame-wise AR is unambiguously defined, and it therefore provides the controlled setting required to establish and validate the pipeline. Direct generalisation to multi-canal, multi-rooted or markedly curved canals accordingly warrants further validation, and the extension of the framework to those configurations is the subject of ongoing work for which the present study is intended as the methodological foundation.

Although a high level of agreement was observed between manual and automated AR measurements (ICC = 0.935; 95% CI = 0.858-0.969), both Passing–Bablok regression (slope = 1.119, 95% CI = 1.032-1.254; intercept = −0.129, 95% CI = −0.342 to −0.005) and Deming regression (slope = 1.181, 95% CI = 0.966-1.330) demonstrated a proportional tendency towards higher automated values at larger measurements, and regression of the Bland–Altman differences on their means confirmed this (slope = 0.162, $P = .009$).[22,23] This modest upward bias is likely attributable to sub-pixel contour interpolation and ellipse fitting procedures inherent to the automated framework, which may capture boundary transitions with marginally greater sensitivity than manual measurements. A second contributing factor is that the morphological dilation applied during mask refinement expands the segmented boundary by a fixed number of pixels, which represents a proportionally larger increment on the major axis of an elongated canal than on a near-circular one; both mechanisms predict the direction of bias observed. Because the proportional component is statistically supported rather than incidental, the authors do not describe the 2 methods as interchangeable. The bias is small relative to the measured range and does not affect the relative ordering of specimens, so the automated output is suitable for morphometric grouping and for comparisons made within the framework; however, absolute AR values obtained by the 2 methods should not be pooled, and values in the elongated range should be converted using the regression relationship reported in the Results before being compared with manually acquired data.

Future research may incorporate machine-learning–based segmentation to reduce threshold dependency, and non-elliptical contour descriptors such as spline-based boundary modelling or Fourier shape descriptors may improve irregular geometry capture. Multi-level manual validation across coronal, middle and apical thirds, development of a multi-contour version of the pipeline capable of tracking branching canal systems, and testing on independent samples from different populations are the immediate priorities. Integration of full 3D reconstruction from video-based inputs, comparison with micro-CT volumetric ground truth, and in vivo validation could further strengthen clinical relevance. Real-time

implementation embedded in microscope or chairside imaging platforms could transform this workflow into an interactive digital endodontics tool, supporting diagnosis, training and adaptive preparation strategies.

Beyond morphometric quantification, the integration of DTW clustering revealed 3 distinct anatomical behaviour patterns, indicating that temporal evolution of canal geometry can be used as a discriminative anatomical marker. These outcomes highlight the potential of time-series–based morphometric analysis not only for anatomical research, but also for future digital endodontic applications such as shaping strategy planning, instrument design optimisation and training simulations.

Further work incorporating larger datasets, machine-learning-driven segmentation, and extension to multi-rooted teeth may strengthen clinical translation.[32,33] With continued development, this approach may contribute to anatomy-informed research on canal preparation; any application to real-time intraoperative guidance would require prospective clinical validation beyond the scope of the present laboratory study.

CONCLUSIONS

The computer vision–based canal analysis framework successfully quantified morphological parameters including AR, R, and FF along continuous axial sections, and automated AR measurements showed good to excellent agreement with manual reference measurements at the CEJ (ICC = 0.935; 95% CI = 0.858-0.969), with a small but statistically supported proportional bias; R and FF were not subjected to formal method comparison. The analysis demonstrated that canal elongation and morphological complexity peaked predominantly within the middle third rather than gradually increasing towards the apex, in agreement with micro-CT studies on mandibular incisors. Dynamic time warping–based clustering of AR trajectories resolved 3 reproducible morphological strata within each root third—round, transitional and flattened—in a tooth type conventionally regarded as anatomically simple, while showing that stratum membership is not conserved along the root. This method provides a reproducible approach for quantitative canal morphology assessment within the limits of the validation performed and establishes the methodological basis for extending continuous morphometric profiling to multicanal and multi-rooted configurations.

Data Availability Statement: The morphometric data supporting the findings of this study are provided within the article and its Supplementary Material, which reports the full comparison of the candidate clustering solutions. The analysis code is not publicly deposited, as the pipeline is under continued development and forms the methodological basis of ongoing work extending the framework to multi-canal and multi-rooted configurations. All parameters, thresholds, libraries and procedural steps required to re-implement the workflow are reported in full in the Materials and Methods. The analysis code and the specimen-level cluster assignments underlying Supplementary Material are available from the corresponding author on reasonable request for the purposes of non-commercial academic verification.

Ethics Committee Approval: Ethical committee approval was received from the Ethics Committee of the Universiti Malaya (Approval no: DF RD2411/0075 (L); Date: 27.08.2024).

Informed Consent: Not applicable.

Peer-review: Externally peer-reviewed.

Author Contributions: Concept – A.T., M.H.H., H.M.A.E., H.M.A.A.; Design – A.T., M.H.H., H.M.A.E., H.M.A.A.; Supervision – M.H.H., H.M.A.A.; Resources – A.T., M.H.H., H.M.A.E., H.M.A.A.; Materials – A.T., M.H.H., H.M.A.E., H.M.A.A.; Data Collection and/or Processing – A.T., M.H.H., H.M.A.E., H.M.A.A.; Analysis and/or Interpretation – A.T., M.H.H., H.M.A.E., H.M.A.A.; Literature Search – A.T., H.M.A.A.; Writing – A.T., H.M.A.A.; Critical Review – A.T., M.H.H., H.M.A.E., H.M.A.A.

Declaration of Interests: The authors have no conflicts of interest to declare.

Funding: The authors declare that this study received no financial support.

REFERENCES

1. Vertucci FJ. Root canal morphology and its relationship to endodontic procedures. *Endod Top*. 2005;10(1):3-29. [CrossRef]
2. Versiani MA, Martins JNR, Ordinola-Zapata R. Anatomical complexities affecting root canal preparation: a narrative review. *Aust Dent J*. 2023;68(suppl 1):S5-S23. [CrossRef]
3. Tang Y, Wu Y, Pei F, et al. A micro-computed tomographic analysis of the root canal systems in the permanent mandibular incisors in a Chinese population. *BMC Oral Health*. 2023;23(1):129. [CrossRef]
4. Kaur K, Saini RS, Vaddamanu SK, et al. Exploring technological progress in three-dimensional imaging for root canal treatments: a systematic review. *Int Dent J*. 2025;75(2):1097-1112. [CrossRef]
5. Ahmed HMA. A critical analysis of laboratory and clinical research methods to study root and canal anatomy. *Int Endod J*. 2022;55(suppl 2):229-280. [CrossRef]
6. Haberthür D, Hlushchuk R, Wolf TG. Automated segmentation and description of the internal morphology of human permanent teeth by means of micro-CT 2020.10.27.356998. *bioRxiv*. 2020. [CrossRef]
7. Farhan M, Hutagalung SMHSM, Rasyid M, et al. Real-time object color detection using the HSV method in python. In: Prosiding Seminar Nasional Ilmu Komputer, Sosial Sains, Teknik dan Multi-Disiplin Ilmu; 2025:1-5.
8. Filpo-Perez C, Bramante CM, Villas-Boas MH, Húngaro Duarte MA, Versiani MA, Ordinola-Zapata R. Micro-computed tomographic analysis of the root canal morphology of the distal root of mandibular first molar. *J Endod*. 2015;41(2):231-236. [CrossRef]
9. Ordinola-Zapata R, Martins JNR, Versiani MA, Bramante CM. Micro-CT analysis of danger zone thickness in the mesiobuccal roots of maxillary first molars. *Int Endod J*. 2019;52(4):524-529. [CrossRef]
10. Ahmed HMA, Versiani MA, De-Deus G, Dummer PMH. A new system for classifying root and root canal morphology. *Int Endod J*. 2017;50(8):761-770. [CrossRef]
11. Suzuki S, Abe K. Topological structural analysis of digitized binary images by border following. *Comput Vis Graph Image Process*. 1985;30(1):32-46. [CrossRef]
12. Fitzgibbon AW, Pilu M, Fisher RB. Direct least squares fitting of ellipses. In: *Proceedings of the 13th International Conference on Pattern Recognition*. Institute Of Electrical And Electronics Engineers; New York. 1996;253-257 vol.1. [CrossRef]
13. Sevgi U, Johnsen GF, Hussain B, Piasecki L, Nogueira LP, Haugen HJ. Morphometric micro-CT study of contralateral mandibular incisors. *Clin Oral Investig*. 2023;28(1):20. [CrossRef]
14. Versiani MA, Keleş A Orhan K, ed. *Micro-computed Tomography (Micro-CT) in Medicine and Engineering*. Springer International Publishing; Cham; 2020:183-211. [CrossRef]
15. Sakoe H, Chiba S. Dynamic programming algorithm optimization for spoken word recognition. *IEEE Trans Acoust Speech Signal Process*. 1978;26(1):43-49. [CrossRef]
16. Glock AC, Chmelina K, Fürnkranz J, Hütter T. Dynamic time warping for classifying long-term trends in time series. *Data Knowl Eng*. 2026;161:102495. [CrossRef]
17. Milligan GW, Cooper MC. An examination of procedures for determining the number of clusters in a data set. *Psychometrika*. 1985;50(2):159-179. [CrossRef]
18. Tavenard R, Faouzi J, Vandewiele G, et al. Tslearn, A machine learning toolkit for time series data. *J Mach Learn Res*. 2020;21(118):1-6.
19. Bradski G. The opencv library. *Dr Dobbs J Softw Tools Prof Programmer*. 2000;25:120-123.

20. OpenCV Team. OpenCV modules. OpenCV Documentation; 2025. https://docs.opencv.org/4.12.0/. Accessed 11 November 2025.
21. Howse J, Minichino J. Learning OpenCV 4 Computer Vision with Python 3: Get to Grips with Tools, Techniques, and Algorithms for Computer Vision and Machine Learning. Birmingham, UK: Packt Publishing Ltd; 2020.
22. Bland JM, Altman DG. Statistical methods for assessing agreement between two methods of clinical measurement. *Lancet*. 1986;1(8476):307-310. [CrossRef]
23. Passing H, Bablok W. A new biometrical procedure for testing the equality of measurements from two different analytical methods. Application of linear regression procedures for method comparison studies in clinical chemistry, Part I. *J Clin Chem Clin Biochem*. 1983;21(11):709-720. [CrossRef]
24. Chen M, Wang H, Tsauo C, et al. Micro-computed tomography analysis of root canal morphology and thickness of crown and root of mandibular incisors in Chinese population. *Clin Oral Investig*. 2021;26(1):901-910. [CrossRef]
25. Ahmed HMA, Noor NSM, Hasanusi HFB, et al. Characterisation of root canal configurations and accessory canals in mandibular incisors: a micro-computed tomography study on a Malaysian subpopulation. *Aust Endod J*. 2025;51(2):258-266. [CrossRef]
26. Lima CO, Silva EJNL, Maciel LV, Montan JB, Barbosa AFA, Versiani MA. Morphometric mapping of mandibular incisor root canals and its implications for instrument size-taper selection. *J Endod*. 2026;52(7):1186-1193. [CrossRef]
27. Kasahara N, Yamada M, Fujii R, et al. Morphological classification of mandibular central incisor root canals and incidence of accessory root canals in Japanese people using micro-computed tomography. *J Hard Tissue Biol*. 2025;34(2):57-62. [CrossRef]
28. Leoni GB, Versiani MA, Pécora JD, Damião de Sousa-Neto MD. Micro-computed tomographic analysis of the root canal morphology of mandibular incisors. *J Endod*. 2014;40(5):710-716. [CrossRef]
29. Plotino G, Ahmed HMA, Grande NM, Cohen S, Bukiet F. Current assessment of reciprocation in endodontic preparation: a comprehensive review—Part II: properties and effectiveness. *J Endod*. 2015;41(12):1939-1950. [CrossRef]
30. Martins JNR, Silva EJNL, Marques D, et al. Comparison of five rotary systems regarding design, metallurgy, mechanical performance, and canal preparation-a multimethod research. *Clin Oral Investig*. 2021;26(3):3299-3310. [CrossRef]
31. Wang H, Yang X, Zou L, et al. Shaping outcome of ProTaper NEXT for root canal preparation in mandibular incisors: a micro-CT study. *BMC Oral Health*. 2022;22(1):302. [CrossRef]
32. Ahmed HMA, Al-Maswary A, Habaebi MH, et al. Artificial intelligence in the study of root and canal anatomy: a comprehensive review on applications, advantages, challenges and future directions. *Eur Endod J*. 2025;10(5):343-364. [CrossRef]
33. Mohammad-Rahimi H, Sohrabniya F, Ourang SAH, et al. Artificial intelligence in endodontics: data preparation, clinical applications, ethical considerations, limitations, and future directions. *Int Endod J*. 2024;57(11):1566-1595. [CrossRef]

SUPPLEMENTARY MATERIAL

Supplementary Methods. Determination of the number of clusters (k)

Aspect-ratio trajectories were clustered separately for the coronal, middle and apical thirds using K-medoids applied to the pairwise Dynamic Time Warping (DTW) distance matrix, with a fixed random seed to ensure deterministic partitions. Solutions for k = 2, 3, 4 and 5 were generated from the identical distance matrix and compared before a final value was adopted.

No single internal validity index is decisive for the clustering of morphological time series, and indices of this type are known to favour different solutions depending on cluster shape and separation.[17] The number of clusters was therefore determined by the convergence of three criteria, each addressing a different requirement of the intended application: (i) the population of the resulting clusters, since groups containing very few specimens cannot support morphological interpretation or subsequent comparative use; (ii) the consistency of cluster assignment between root thirds, since a partition intended to describe canal-wide morphology should not reorganize completely from one root level to the next; and (iii) the nested behaviour of the partitions, that is, whether increasing k revealed an additional morphological phenotype or merely subdivided an existing group along the same morphological axis.

Conclusion of the k-selection analysis

The three criteria converge on k = 3. Two clusters were insufficient to represent the transitional morphology lying between predominantly round and markedly flattened canals, and produced partitions that were not consistent between the middle and apical thirds. Four and five clusters generated sparsely populated groups (as few as 8% of the sample) that arose by subdividing an existing group along the same morphological axis, without adding an interpretable phenotype. The three-cluster solution retained well-populated groups in every root third, showed the most consistent assignment across root levels, and corresponded to morphologically distinguishable phenotypes: a predominantly round, a transitional, and a markedly elongated or flattened canal type.

Supplementary Table 1. Cluster size distribution for k = 2–5 in each root third (n = 50 specimens)

k / Root third	Cluster sizes (n of 50)	Smallest cluster n (%)	All clusters ≥ 20% of sample
k = 2 Coronal	19, 31	19 (38%)	Yes
k = 2 Middle	23, 27	23 (46%)	Yes
k = 2 Apical	31, 19	19 (38%)	Yes
k = 3 Coronal	17, 15, 18	15 (30%)	Yes
k = 3 Middle	12, 16, 22	12 (24%)	Yes
k = 3 Apical	18, 19, 13	13 (26%)	Yes
k = 4 Coronal	17, 4, 11, 18	4 (8%)	No
k = 4 Middle	13, 7, 18, 12	7 (14%)	No
k = 4 Apical	18, 16, 5, 11	5 (10%)	No
k = 5 Coronal	17, 4, 5, 10, 14	4 (8%)	No
k = 5 Middle	13, 8, 12, 9, 8	8 (16%)	No
k = 5 Apical	10, 15, 9, 5, 11	5 (10%)	No

Solutions with k ≥ 4 produced clusters containing as few as four specimens (8% of the sample) in the coronal third and five specimens (10%) in the apical third. k = 3 is the largest value at which every cluster in every root third retained at least 12 specimens (≥ 24% of the sample)

Supplementary Results. Cross-sectional shape categories and DTW distance statistics by root third

The two analyses below were computed on the full frame-level dataset (8,334 valid cross-sections from 50 specimens) and are independent of the clustering solution: the aspect ratio–based shape classification is applied frame by frame, and the DTW distance matrix is derived from the trajectories themselves. They are reported as descriptive support for the finding that morphological complexity peaks in the middle third.

Supplementary Table 2. Consistency of cluster assignment between root thirds (adjusted Rand index, ARI)

k	Coronal–Middle	Middle–Apical	Coronal–Apical	Mean ARI	Identical label in all three thirds
2	0.452	−0.005	−0.020	0.142	23/50 (46%)
3	0.342	0.085	0.099	0.176	17/50 (34%)
4	0.223	0.097	0.095	0.138	15/50 (30%)
5	0.249	0.152	0.071	0.158	11/50 (22%)

A higher ARI indicates that specimens grouped together in one root third tend to remain grouped together in another. Averaged across the three pairwise comparisons, k = 3 produced the most consistent assignment across root levels. The k = 2 solution achieved a high coronal–middle ARI but essentially no agreement between the middle and apical thirds, indicating that a two-group partition captures a coronal contrast rather than a canal-wide morphological pattern.

Supplementary Table 3. Nested relationship between the k = 3 and k = 4 solutions (cross-tabulation of specimen counts)

Coronal third				
k = 3	k = 4 C1	k = 4 C2	k = 4 C3	k = 4 C4
Cluster 1	17	0	0	0
Cluster 2	0	4	11	0
Cluster 3	0	0	0	18
Middle third				
k = 3	k = 4 C1	k = 4 C2	k = 4 C3	k = 4 C4
Cluster 1	10	0	2	0
Cluster 2	3	7	6	0
Cluster 3	0	0	10	12
Apical third				
k = 3	k = 4 C1	k = 4 C2	k = 4 C3	k = 4 C4
Cluster 1	18	0	0	0
Cluster 2	0	16	3	0
Cluster 3	0	0	2	11

In every root third the k = 4 solution was obtained by subdividing one of the three existing groups rather than by identifying an additional phenotype. In the coronal third the intermediate group (k = 3 Cluster 2) was split into subgroups of 4 and 11 specimens; in the middle and apical thirds the elongated group (k = 3 Cluster 3) was split. The additional partition therefore separated specimens differing in degree along the same morphological axis rather than in kind, and did not yield a fourth interpretable canal phenotype.

Supplementary Table 4. Distribution of aspect ratio–based cross-sectional shape categories by root third (n = 8,334 frames)

Root third	Frames (n)	Round[a]	Oval	Long Oval	Flattened
Coronal	2,777	103 (3.7%)	1,463 (52.7%)	1,109 (39.9%)	102 (3.7%)
Middle	2,758	16 (0.6%)	959 (34.8%)	1,502 (54.5%)	281 (10.2%)
Apical	2,799	52 (1.9%)	1,795 (64.1%)	878 (31.4%)	74 (2.6%)

[a]The classification of Jou et al. is retained without modification; in the original scheme the Round class is defined by the limiting value AR = 1.000. Because aspect ratio is measured as a continuous variable at sub-pixel resolution this value is effectively unattainable (the smallest value recorded across the 8,334 analysed cross-sections was 1.0018), and applying the definition literally would leave the class permanently empty for reasons of measurement rather than of anatomy. An operational tolerance of AR ≤ 1.05 was therefore adopted for frame assignment. It is a pragmatic convention rather than a measurement-resolved boundary: it is smaller than the mean absolute difference between manual and automated measurement (0.124), so genuinely oval cross-sections are not drawn into the Round class, but it is also smaller than the measurement uncertainty itself, and frames in this band should be read as approximately circular rather than as a category reliably separable from Oval. The boundaries at AR = 2.0 and AR = 4.0 are unchanged. The middle third contained the lowest proportion of Round and Oval cross-sections and the highest proportion of Long Oval and Flattened cross-sections, whereas the apical third was the most circular region of the canal. The proportion of Flattened cross-sections was approximately three times higher in the middle third than in the coronal third and approximately four times higher than in the apical third. Round cross-sections were correspondingly scarce at mid-root (0.6% of frames) compared with the coronal (3.7%) and apical (1.9%) thirds. This frame-level distribution independently reproduces, at the level of individual cross-sections, the mid-root peak in aspect ratio observed in the cluster-level analysis

Supplementary Table 5. Pairwise DTW distance statistics for aspect-ratio trajectories, by root third

Root third	Min	Max	Mean	SD	Median	95th pct	99th pct
Coronal	0.24	28.94	6.63	5.00	5.47	16.15	26.40
Middle	0.78	32.44	8.59	6.14	6.91	21.86	28.23
Apical	0.37	20.91	5.66	4.12	4.28	13.77	17.01
Whole canal	1.09	44.25	8.99	6.29	7.39	21.88	31.69

Statistics were computed on the raw DTW distance matrix using the unique pairwise distances only (upper triangle, n(n−1)/2 = 1,225 pairs for 50 specimens); self-distances and duplicated pairs are excluded. Pairwise DTW distance quantifies the dissimilarity between the aspect-ratio trajectories of two specimens over the region concerned, so larger values indicate greater between-specimen morphological heterogeneity. The middle third showed the highest mean (8.59) and the greatest dispersion (SD 6.14; 95th percentile 21.86; maximum 32.44) of the three root regions, while the apical third was the most homogeneous (mean 5.66; SD 4.12; maximum 20.91) and the coronal third occupied an intermediate position (mean 6.63; SD 5.00). Mean pairwise dissimilarity in the middle third exceeded that of the apical third by 52% and that of the coronal third by 30%. These values provide the quantitative basis for the statement in the Discussion that the middle third represents the zone of greatest geometric heterogeneity along the canal pathway.